Numerical-Simulation-Driven Optimization of a Laser Transmission Welding Process Under Consideration of Scattering

Xiao Wang, Hao Chen, Huixia Liu

School of Mechanical Engineering, Jiangsu University, Zhenjiang 212013, China
Correspondence to: X. Wang (E-mail: wx@ujs.edu.cn)

ABSTRACT: In this study, because the use of semicrystalline polypropylene (upper material) leads to the scattering of laser radiation, an integrated method for a numerical-simulation-driven optimization of the laser transmission welding (LTW) process was investigated through the finite element method (FEM), response surface methodology (RSM), and experiments (EX). First, EX for measuring the actual laser power and spot diameter within the weld interface were conducted; these were used to simulate the temperature field and molten pool geometric characteristic parameters of the LTW process. Then, central composite design was used to design the EX, and RSM was used to establish mathematical models. Finally, the desirability function was used to determine the optimal process parameters. The experimental results nearly agreed with the simulated and predicted values. The results illustrate that the integrated (FEM–RSM–EX) approach was an effective optimization method and could play a significant guiding role in LTW EX and in quickly optimizing the process parameters. © 2014 Wiley Periodicals, Inc. J. Appl. Polym. Sci. **2014**, *131*, 40396.

INTRODUCTION

Recently, the laser transmission welding (LTW) of polypropylene (PP) has become a focus of research. Polypropylene has the features of being nontoxic, tasteless, and lightweight and easily forming complex shapes; it is widely used in several industries and is considered to be difficult to weld. However, LTW technology has been able to overcome this problem.[1–6]

In the last decade, with the development of numerical methods, namely, response surface methodology (RSM), genetic algorithms, artificial neural networks, and so on, which are modeling and optimization methods for developing mathematical models and determining the optimal process parameters of the LTW process. Wang et al.[7] established mathematical relationships between the joining process parameters and the desired responses. The multiobjective optimization of the joining process parameters was carried out, and the results of the optimization nearly agreed with the experimental results. Acherjee et al.[8] developed mathematical models to establish the relationships between the welding process parameters and the responses. A numerical multiobjective optimization technique of RSM was used to find the optimal parameters, and a graphical optimization technique was also applied.

As is known, the previous methods can be used to predict the welding properties of the LTW adequately and enhance the welding quality on the basis of a large number of experiments (EX).

However, doing EX of welding is time-consuming and ineffective. On the other hand, with the popularization of high-speed computers and with the evolution of numerical simulation technology, more and more researchers have chosen the finite element method (FEM), which can save time and effort in the simulation and analysis of the LTW process. Mayboudi et al.[9] set up a three-dimensional transient thermal model for unreinforced nylon 6 specimens in the LTW process. Heat conduction along the direction of welding was taken into account. Mahmood et al.[10] set up a three-dimensional thermal model to determine the optimal conditions of the joining of titanium and polyimide. The numerical model was confirmed with EX, and good agreement was found. Mian et al.[11] set up an uncoupled, three-dimensional thermal model to join glass and polyimide. In this model, the temperature distribution within the substrates was calculated as a function of time. Acherjee et al.[12] set a three-dimensional model to simulate the laser transmission contour welding process by a volumetric Gaussian heat source. Then, mathematical models were developed on the basis of simulated results, and sensitivity analysis was used to study the relationships between the process parameters and the output parameters.

In a review of past literature, some of the studies used welding EX to guide experimental design, develop mathematical models, and optimize the process parameters. However, the use of EX to determine the optimal process parameters is a time-consuming
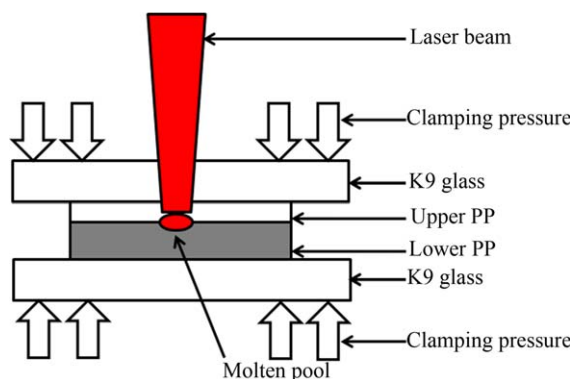
Figure 1. Schematic of the LTW process. [Color figure can be viewed in the online issue, which is available at wileyonlinelibrary.com.]

and high-cost project. Others have used numerical simulation methods to reduce the number of welding EX, and most of the simulations have been devoted to the development of thermal models to predict the temperature field and welding characteristics where scattering is ignored. So far, no numerical simulation has been involved in the experimental design; thus, the number of welding EX is hard to reduce. In this study, an efficient and comprehensive approach was used to investigate the numerical-simulation-driven optimization of the LTW process with scattering considered, and we studied the influence of the ratio of the molten pool depth to the welding material thickness (D/T) on the shear strength (SS). Meanwhile, numerical simulation was involved in the experimental design.

EXPERIMENTAL

In this study, the materials used were 2 mm thick semicrystalline (semitransparent) PP (the upper PP) filled with 10% glass fibers and 3.5 mm thick opaque PP (the lower PP) filled with 20% carbon fibers. These were available from Westlake Plastics Co. (Lenni, PA). The melt flow index of the glass-fiber-reinforced PP was 8.73 g/10 min, whereas that of the carbon-fiber-reinforced PP was 4.93 g/10 min. Meanwhile, the grade count of the glass-fiber-reinforced PP was 74, whereas that of the carbon-fiber-reinforced PP was 4.They were welded by means of a continuous wave radiation with a near-IR diode laser. Figure 1 shows the schematic diagram of the LTW process, and K9 glass is a kind of optical glass whose light transmittance is more than 90%.

MEASUREMENTS OF THE EXPERIMENTAL WORK AND THEORETICAL DESCRIPTION OF PHOTON SCATTERING

Because of the effect of scattering, the actual spot diameter (AD) of the laser beam within the weld interface was expanded, and the laser power (P) decreased. The measurement EX were conducted to characterize the actual laser power (AP) and AD within the weld interface. The measuring setup and procedures used in the EX are described in detail later.

Experimental Setup

A Compact 130/140 semiconductor continuous laser manufactured by Dilas for the welding EX was used in this study. The maximum power of the laser device was 130 W, the output

wavelength was 980 ± 10 nm, the core of the optical fiber was 400 nm, and the numerical aperture was 0.22 μm, and the minimum diameter of the laser beam was 700–800 μm.

In this study, a UP55N-300F-H12-D0 power meter made in Canada was used to measure the AP within the weld interface directly. Moreover, a controlled electronic universal testing machine was used for the tensile testing EX to obtain the SS values of the welded samples. The tensile testing EX were conducted at 20°C with a crosshead speed of 0.5 mm/min, and the SS was calculated as the maximum load to failure per unit area of the weld, which is shown later:

$$SS = \frac{T}{WW \times L} \tag{1}$$

where T is the tensile load, WW is the weld width, and L is the width of the specimen.

Theoretical Description of Photon Scattering

Scattering occurs when a photon hits a particle that is nonabsorbent. The direction of scattering is chosen according to the normalized phase function supplied by Mie theory, which represents the probability density function for the longitudinal and azimuthal angles.

The direction of scattering is defined by two angles (θ and φ), which are relative to the incident direction. With unpolarized radiation and spherical particles, there is no azimuthal dependence with phase function, so φ is uniformly distributed between 0 and 2π:[13]

$$\varphi = 2\pi\xi \tag{2}$$

where ξ is a pseudo-random number, which is uniformly distributed over the interval [0,1].

θ is chosen to use the phase function, which is given a pseudo-random number through the inversion of the following integral:

$$\xi = \frac{\int_0^\theta p(\theta)\sin(\theta)d\theta}{\int_0^\pi p(\theta)\sin(\theta)d\theta} \tag{3}$$

where p is known as the phase in the light-scattering literature.

Characterization of AP and AD Within the Weld Interface

Because once the laser beam started to pass through the upper PP, the power within the weld interface was lower than the one that was given by the semiconductor continuous laser due to scattering. To measure the AP within the weld interface, the method using the measurement system is illustrated schematically in Figure 2. As shown, a laser beam was emitted; it passed through the upper PP and ultimately got absorbed by the power meter. Then, the AP within the weld interface was measured and was displayed in the display device of the power meter.

To measure the AD within the weld interface, a moving laser beam was passed through the upper PP and got absorbed by laser-dimming paper. The lase-dimming paper was assumed to absorb the whole laser energy and makes the paper melt, and small heat-affected zone is negligible. In this measurement system, the width of the melted area on the laser-dimming paper was equivalent to the value of the AD within the weld interface due to scattering. The AD changed with the value of stand-off
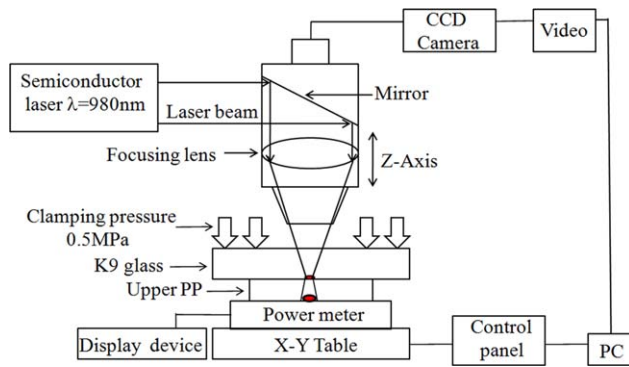
Figure 2. Schematic illustration of the system for measuring AP within the weld interface. [Color figure can be viewed in the online issue, which is available at wileyonlinelibrary.com.]

distance (F), which was the distance between the laser device and work material. The laser beam began to scan through the upper PP; it started at a constant speed (4 mm/s) and power (4 W) with an F of +0 mm. After each scan, F was increased incrementally by an integer value, and a new area was scanned on the laser-dimming paper. As the value of F was increased on subsequent scans, the width of the area that melted on the laser-dimming paper increased, and this is shown in Figure 3. The widths of the melted area on the laser-dimming paper were measured by a three-dimensional VHX-1000 microscope. Table I presents the different values of F and its corresponding ADs within the weld interface.

NUMERICAL SIMULATION OF THE LTW PROCESS

Theoretical Description of the Model

On the basis of the energy conservation law, the following differential equation for the three-dimensional model was considered to model the heat transfer in the LTW process that defined the temperature distribution within the body, and it balanced
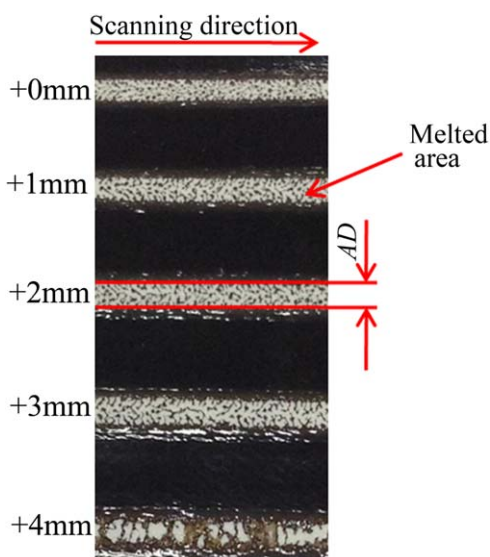
Figure 3. Melt areas after laser-beam scanning through the upper PP. [Color figure can be viewed in the online issue, which is available at wileyonlinelibrary.com.]

the rate of internally generated heat within the body and the rate of thermal conduction to the boundaries:[10]

$$\frac{\partial}{\partial x}\left(k_x \frac{\partial T}{\partial x}\right) + \frac{\partial}{\partial y}\left(k_y \frac{\partial T}{\partial y}\right) + \frac{\partial}{\partial z}\left(k_z \frac{\partial T}{\partial z}\right) + H = \rho c \left(\frac{\partial T}{\partial t} - v \frac{\partial T}{\partial x}\right)$$
(4)

where T is the temperature (K); ρ is the density (kg/m³); t is the time (s); c is the specific heat capacity (J kg⁻¹ K⁻¹); k_x, k_y, and k_z are the thermal conductivities in the x, y, and z directions (W m⁻¹ K⁻¹), respectively; H is the internal heat generation rate per unit volume (W/m³); and v is the speed of the laser (m/s).

The initial condition can be expressed as follows:

$$T(x, y, z, 0) = T_o \qquad (x, y, z) \in D \tag{5}$$

The natural boundary conditions can be written as follows:

$$k_n \frac{\partial T}{\partial n} - q + h(T - T_o) + \sigma\varepsilon(T^4 - T_o^4) = 0 \quad (x, y, z) \in SF \quad t > 0$$
(6)

where SF represents the surfaces attached to the imposed heat fluxes, radiation, and convection; K_n represents the thermal conductivity normal to the boundary welding speed (W m⁻¹ K⁻¹) and n is the normal direction; h is the coefficient of heat convection [W/(m² K)]; σ is defined as the Stefan–Boltzmann constant for radiation (5.67 × 10⁻⁸ W m⁻² K⁻¹⁴); ε is the coefficient of heat radiation; T is the surface temperature of material (K); T_0 is the ambient temperature (K); and q represents the heat flux normal to the boundary welding speed (W/m²). The inclusion of the temperature-dependent thermophysical properties [e.g., c and the number of input variables (k)] and the thermal radiation conditions make this type of temperature field analysis a typical nonlinear problem.

Modeling with ANSYS

Table II presents the thermophysical properties of the upper PP filled with 10% glass fibers and the lower PP filled with 20% carbon fibers used in this study. The material properties used for the finite element analysis were ρ, c, and thermal conductivity (K).[14]

In this study, a three-dimensional model was developed with the finite element software multiphysics solver ANSYS 12.0 to simulate the temperature distribution around the laser-irradiation area. The whole finite element model was meshed by the SOLID 70[15] thermal-brick element, which had eight nodes with a single-temperature degree of freedom (df). Figure 4(a) shows the configuration of the PP dimensions and the lapped portion. To reduce the simulated time, the lapped portion of the PP was used to simplify the finite element model. Figure 4(b) shows the nonuniform mesh pattern. The laser irradiated

Table I. Different Values of F and the Corresponding ADs Within the Weld Interface

Parameter	Notation	Limit				
Standoff distance (mm)	F	+0	+1	+2	+3	+4
Actual spot diameter (mm)	AD	1.16	1.20	1.23	1.26	1.30

Table II. Thermophysical Properties of the PP Used in This Study

Material	ρ (kg/m^3)	c (J kg^{-1} K^{-1})	K (W m^{-1} K^{-1})
PP (10% glass-fiber-reinforced)	900	$\begin{cases} T \leq T_f \Rightarrow C = 1.92\left[1 + 3(T-25)10^{-3}\right] \\ T \succ T_f \Rightarrow C = 2.54\left[1 + 1.4(T-25)10^{-3}\right] \end{cases}$	0.16
PP (20% carbon-fiber-reinforced)	900	$\begin{cases} T \leq T_f \Rightarrow C = 1.92\left[1 + 3(T-25)10^{-3}\right] \\ T \succ T_f \Rightarrow C = 2.54\left[1 + 1.4(T-25)10^{-3}\right] \end{cases}$	1.21

area was meshed with fine meshes because of the heat source focus, whereas the neighboring area of the fine meshes was meshed with the coarse meshes to enhance the calculation accuracy and to reduce the simulated time.

In this study, it was necessary to define a trend for the heat source, and the laser-beam heat source was modeled by a moving super-Gaussian heat source whose intensity was uniform. The heat source was modeled as a distributed plane heat flux $[q(r)]$ in the region near the laser irradiation areas. $q(r)$ was calculated as follows:[16]

$$q(r) = \begin{cases} Q/(\pi r_b^2), & r \leq r_b \\ 0, & r > r_b \end{cases} \quad (7)$$

where r_b is the characteristic radius (defined as the radius where the intensity of the laser beam falls to 5% of the maximum intensity); $r = \sqrt{x_s^2 + y_s^2}$ is the radial distance of any point from the laser-beam center on the surface of the welding material, where x_s and y_s are the Cartesian coordinates of that point; and Q is the power transferred into the material.

In this finite element model, the heat conduction, heat radiation, and heat convection were taken into consideration as the heat flux, along with the direction of welding. The convection coefficient was chosen as 10 W m^{-2} K^{-1}, and the radiation coefficient was chosen as 0.92. Some assumptions were also made for the calculation of the temperature field, which were expressed as follows:[17]

1. An intimate contact was considered between the contacting welding materials of the PP. Isotropic thermophysical behavior was considered during the LTW process.

2. Heat conduction of the PP and the surrounding air and the free convection between the surfaces of the PP were considered. The heating phenomena due to the phase changes were ignored.

RESULTS AND ANALYSIS

In this simulation, the 2 mm thick upper PP was laser-welded to a 3.5 mm thick lower PP with a P of 5.4 W, a welding speed (S) of 2 mm/s, and an F of +4 mm. Through the previous measuring method, the laser beam was focused on the lower PP surface with a power of 3.85 W and an AD of 1.3 mm. The temperature distribution on the lapped (x–y) plane changed quickly with time and space. Figure 5(a) shows the plot of the isothermal contours on the lapped plane at 5 s. We observed that the highest temperature of 342.323°C was achieved at the lapped plane and at the weld interface. In the meanwhile, the isothermal contours appeared as near elliptical, and the highest temperature was not at the forefront of the temperature contours but at the center or slightly later. This was due to the characteristics of the heat source and the effect of heat transfer. Figure 5(b) shows a molten pool of PP (in red in the online figure) at the x–z plane at 5 s. The temperature at the x–z plane was above the melting temperature of PP (170°C). As a result, bonding began to occur between the upper and lower PP. A high welding quality was possible when the highest temperature at the weld interface was above the melting temperature (170°C) but below the decomposition temperature (ca. 450°C) of the PP. As shown in Figure 5(b), the dimensions of the molten pool geometric characteristic parameters [WW, molten depth in upper polypropylene (DU), and molten depth in lower polypropylene (DL)] could be derived.
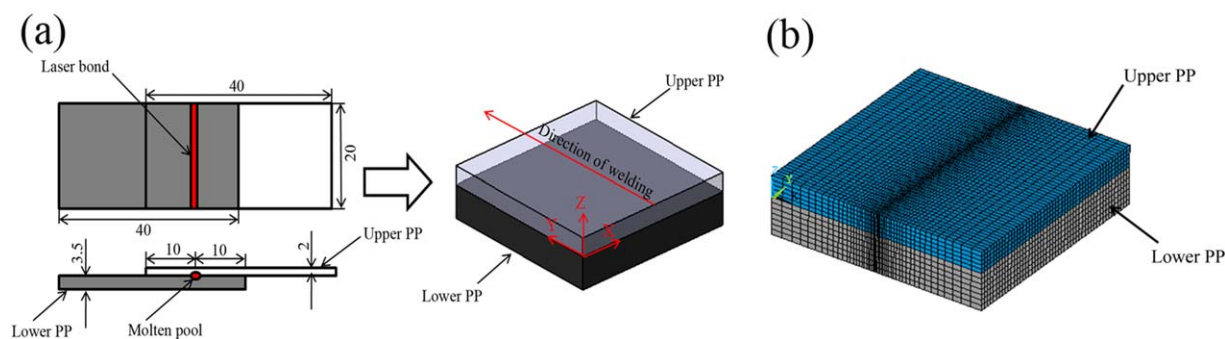
Figure 4. Schematics of (a) the PP dimensions (in millimeters) and the lapped portion and (b) the nonuniform mesh pattern used for the geometrical model of PP. [Color figure can be viewed in the online issue, which is available at wileyonlinelibrary.com.]
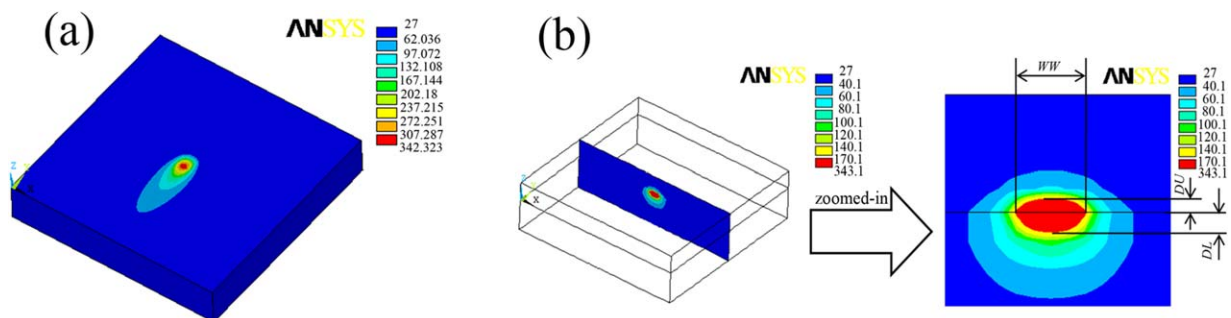
Figure 5. Temperature contours at the (a) lapped (*x–y*) plane at 5 s and (b) *x–z* plane at 5 s. [Color figure can be viewed in the online issue, which is available at wileyonlinelibrary.com.]

Figure 6(a) shows the changing temperature along a line transverse to the welding direction at 5 s. The temperature increased and dropped rapidly along the *x* direction. When the melting temperature of PP was 170°C, the bond started to form at the weld interface when the temperature reached 170°C, so the WW could be determined at the weld interface where the temperature was greater than 170°C. The WW was calculated with the data shown in Figure 6(a), and a value of 1.42 mm for the WW was obtained. Figure 6(b) shows the temperature distribution along the *z* direction at 5 s. The DU and DL also started to form when the temperature in them reached 170°C. As a result, the molten depths could be determined in the PP. With the data from Figure 6(b), the molten depths (DU and DL) could be calculated, and values of 0.265 mm for the DU and 0.400 mm for the DL were obtained.

Verification of the Simulated Molten Pool Geometric Characteristic Parameters with EX

To verify the reliability of the thermal model, three groups of different process parameters were chosen randomly to conduct the confirmation EX. Before the EX, first, acetone was used to

scrub the dirt or stains off the surface of the PP. Then, further cleaning was done with an ultrasonic cleaning machine. Finally, the experimental PP was placed in a dryer for 12 h to remove all of the water and dust. After the EX, all of the welding specimens were observed under a three-dimensional VHX-1000 microscope to measure the molten pool geometric characteristic parameters (WW, DU, and DL).

Table III shows the comparison of the simulated and experimental results of the molten pool geometric characteristic parameters (WW, DU, and DL). We observed that the percentage error between the actual and simulated result was small; in other words, the simulated results were in good agreement with the experimental results. This gave us the confidence to use the current thermal model to simulate the LTW process with acceptable accuracy.

The macrograph and microgram of the welding sample chosen randomly from the EX are presented in Figure 7. As shown, the upper and lower PP were welded together successfully, and the well-proportioned and beautiful weld seam was formed at the weld interface. We also observed that the value of WW was 1.38
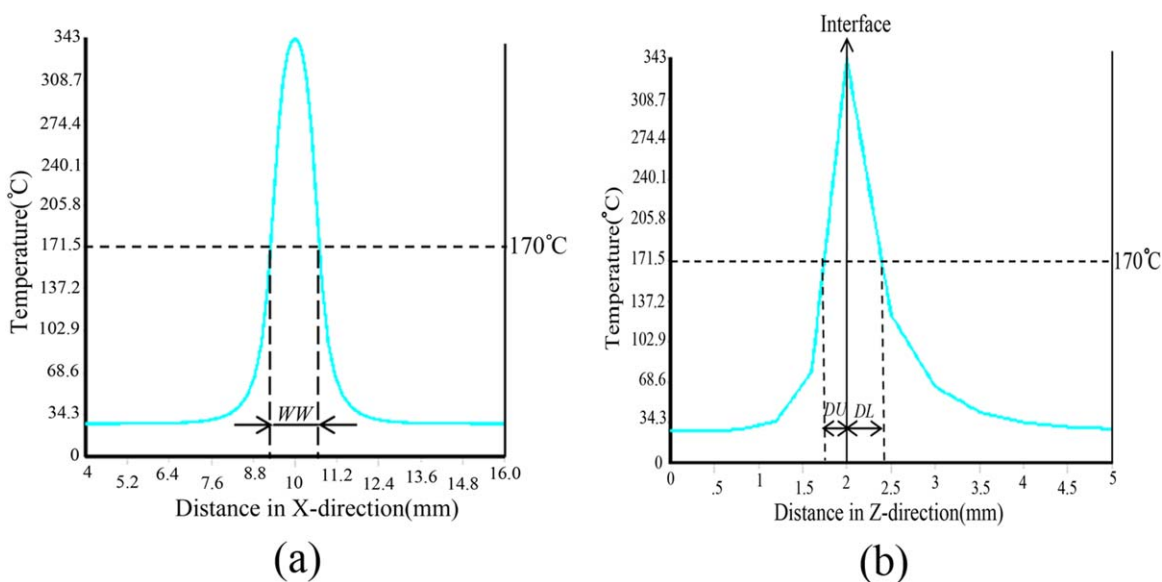
Figure 6. Temperature distribution along the (a) *x* direction at 5 s and (b) *z* direction at 5 s. [Color figure can be viewed in the online issue, which is available at wileyonlinelibrary.com.]

Table III. Comparison of the Simulated and Experimental Results for the Molten Pool Dimensions

Number	P (W)	AP (W)	S (mm/s)	F (mm)		WW (mm)	DU (mm)	DL (mm)
1	4.2	2.90	1	+3	Actual	1.44	0.282	0.450
					Simulated	1.50	0.295	0.465
					|Error|	4.17%	4.60%	3.33%
2	5.0	3.45	2	+2	Actual	1.35	0.255	0.374
					Simulated	1.42	0.270	0.400
					|Error|	5.19%	5.88%	6.95%
3	6.4	4.45	3	+4	Actual	1.26	0.213	0.329
					Simulated	1.35	0.230	0.345
					|Error|	7.14%	7.98%	4.64%

mm and the value of the DU and DL were 0.238 and 0.365 mm, respectively. Meanwhile, the shapes of the molten pool in the upper and lower PP both had semi-oval profiles.

NUMERICAL-SIMULATION-DRIVEN EXPERIMENTAL DESIGN AND MATHEMATICAL MODELING WITH RSM

RSM

RSM is a collection of mathematical and statistical techniques that are helpful for designing EX, developing mathematical models, analyzing problems in which the desired responses are influenced by several variables, and optimizing the desirable responses.[18] RSM uses low- or high-order polynomials used to estimate the response of a practical analysis code. In general, a second-order polynomial used in RSM can be expressed as follows:

$$y = \beta_0 + \sum_{j=1}^{k} \beta_j x_j + \sum_{j=1}^{k} \beta_{jj} x_j^2 + \sum_{i<j} \sum_{j=2}^{k} \beta_{ij} x_i x_j \quad (8)$$

where y is the predicted response value, x_i and x_j are the set of input variables, and β_0, β_j, β_{jj}, and β_{ij} are polynomial coefficients.

Numerical-Simulation-Driven Experimental Design

In this study, three key process parameters that determined the quality of the LTW process were P, S, and stand-off distance

(F). The experiment was designed on the basis of a three-factor, five-level central composite design (CCD) with full replication. Four responses of interest, namely, WW, molten depths in the upper and lower polypropylene (DUL), D/T ratio, and SS were considered as the output variables. The statistical software Design-Expert version 8 was used to conduct statistical analysis, develop mathematical models, and optimize the process parameters. The ranges and levels of the selected process parameters and the units, limits, and notations investigated in this study are given in Table IV. The CCD matrix of the variables and their corresponding results are listed in Table V. In Table V, we list the results of WW and DUL from numerical simulation, the value of D/T from math calculation, the results of SS from the EX of tensile tests, and the results of standard deviation (SD) for the SS from math calculation. The tensile tests were performed transversally to the direction of laser welding. They were repeated three times for each group, and 60 specimens were used in the tensile tests. These were made according to EN ISO 527-1:2012.[19] The actual result of SS was calculated as the average of three tensile tests. In Table V, the total number of independent design points added up to 20, and it can be seen that the heat input to the PP was not enough, and no melting occurred at the weld interface in the first experiment. The WW, DUL, D/T, and SS values were used to evaluate the welding quality. As shown in Table V, the maximum SS was 9.27 MPa,
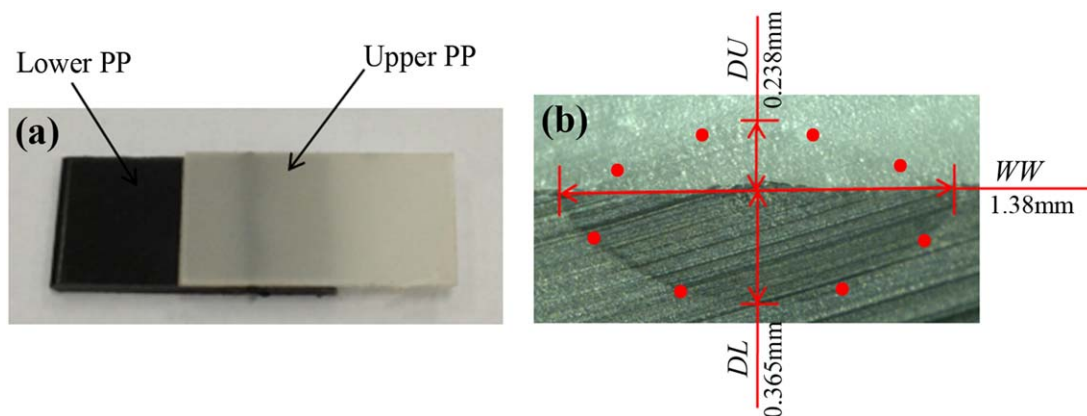
Figure 7. (a) Macrograph of a welding sample and (b) microgram of the WW and molten depths. [Color figure can be viewed in the online issue, which is available at wileyonlinelibrary.com.]

Table IV. Process Control Parameters and Their Limits

Parameter	Notation	Limit				
		−2	−1	0	+1	+2
Laser power (W)	P (AP)	2.5 (1.75)	4.5 (3.25)	6.5 (4.65)	8.5 (6.10)	10.5 (7.7)
Welding speed (mm/s)	S	1	2	3	4	5
Stand-off distance (mm)	F	+0	+1	+2	+3	+4

and the corresponding WW and DUL were 1.50 and 0.695 mm, respectively.

Development of the Mathematical Models

For WW, DUL, and SS, the fit summary recommends the quadratic models, where the additional terms are significant and the models are not aliased.[20] The analysis of variance (ANOVA) tables of the quadratic models are given in Table VI. According to the results in Table VI, the p value of the three responses was less than 0.05, respectively; this indicated that the three models were all statistically significant. The value for the three responses of adequate precision ratio was greater than 4, respectively, and this indicated that all of the models showed adequate discrimination.[21] In addition, the other adequacy measures, R^2, adjusted R^2, and predicted R^2, of the responses were all in reasonable agreement and were close to 1; this indicated the adequacy of the models.[22]

The final mathematical models for WW, DUL, and SS, which could be used for prediction within the limited factors considered in this study, are given as follows:

$$WW = 1.22651 + 0.21353P - 0.41362S + 0.043839F$$
$$+ 9.375e - 3PS - 0.01096P^2 + 0.032634S^2 - 0.013616F^2$$
$$DUL = 0.50268 + 0.20056P - 0.35518S + 0.025714F$$
$$- 9.70982e - 3P^2 + 0.036071S^2 - 9.55357e - 3F^2$$
$$SS = 1.56825 + 1.14076P + 1.76208S - 0.51375F$$
$$+ 0.79PS - 0.24507P^2 - 1.12556S^2$$

Influence of the D/T Ratio on the SS

In this study, the influence of the D/T ratio on SS was also systemically investigated. Figure 8 shows a matching curve of the D/T ratio and the SS with the data from Table V. As shown in Figure 8, the value of SS increased with increasing D/T ratio up to a maximum value and then decreased. The SS attained its greatest value (9.27 MPa) when the specific value of the D/T ratio was 0.1264. When the value of the D/T ratio was less than 0.1264, the SS gradually increased. This was due to the fact that when the effects of the different process parameters resulted in an increase in the laser energy density and caused more heat input to the weld zone, a good welding bond was formed.

Table V. Design Matrix and Responses of Interest

Number	P (W)	S (mm/s)	F (mm)	WW (mm)	DUL (mm)	D/T	SS (MPa)	SD (%)
1	2.5	3	+2	—	—	—	—	—
2	4.5	2	+1	1.38	0.635	0.1155	8.84	9.26
3	4.5	4	+1	1.04	0.425	0.0773	4.13	7.42
4	4.5	2	+3	1.35	0.610	0.1110	5.11	6.84
5	4.5	4	+3	1.02	0.350	0.0636	3.33	4.89
6	6.5	1	+2	1.88	1.135	0.2064	3.11	6.65
7	6.5	5	+2	1.22	0.500	0.0909	4.43	7.81
8	6.5	3	+0	1.36	0.640	0.1164	8.35	11.13
9	6.5	3	+4	1.37	0.630	0.1145	7.52	9.87
10	6.5	3	+2	1.42	0.670	0.1218	8.35	8.47
11	6.5	3	+2	1.42	0.670	0.1218	8.18	7.85
12	6.5	3	+2	1.42	0.670	0.1218	8.04	6.94
13	6.5	3	+2	1.42	0.670	0.1218	8.52	9.28
14	6.5	3	+2	1.42	0.670	0.1218	8.50	10.24
15	6.5	3	+2	1.42	0.670	0.1218	8.28	5.52
16	8.5	2	+1	1.76	0.940	0.1710	4.83	4.35
17	8.5	4	+1	1.50	0.695	0.1264	9.27	8.68
18	8.5	2	+3	1.69	0.895	0.1627	5.58	7.06
19	8.5	4	+3	1.43	0.660	0.1200	6.89	8.67
20	10.5	3	+2	1.64	0.820	0.1490	5.76	7.62

Table VI. ANOVA

Source	Sum of squares	df	Mean square	F	p
WW model[a]					
Model	0.81	7	0.12	260.32	<0.0001
P	0.35	1	0.35	797.51	<0.0001
S	0.39	1	0.39	890.84	<0.0001
F	1.806×10^{-3}	1	1.806×10^{-3}	4.09	0.0682
PS	2.813×10^{-3}	1	2.813×10^{-3}	6.36	0.0283
P^2	0.024	1	0.024	54.11	<0.0001
S^2	0.027	1	0.027	59.97	<0.0001
F^2	4.614×10^{-3}	1	4.614×10^{-3}	10.44	0.0080
Residual	4.862×10^{-3}	11	4.420×10^{-4}		
Pure error	0.000	5	0.000		
Corrected total	0.81	18			
DUL model[b]					
Model	0.55	6	0.092	120.22	<0.0001
P	0.20	1	0.20	259.79	<0.0001
S	0.31	1	0.31	404.12	<0.0001
F	2.500×10^{-3}	1	2.500×10^{-3}	3.28	0.0952
P^2	0.019	1	0.019	24.63	0.0003
S^2	0.032	1	0.032	42.49	<0.0001
F^2	2.272×10^{-3}	1	2.272×10^{-3}	2.98	0.1099
Residual	9.146×10^{-3}	12	7.622×10^{-4}		
Pure error	0.000	5	0.000		
Corrected total	0.56	18			
SS model[c]					
Model	68.12	6	11.35	18.29	<0.0001
P	3.80	1	3.80	6.12	0.0293
S	0.33	1	0.33	0.53	0.4795
F	4.22	1	4.22	6.80	0.0229
PS	19.97	1	19.97	32.18	0.0001
P^2	12.03	1	12.03	19.39	0.0009
S^2	33.17	1	33.17	53.45	<0.0001
Residual	7.45	12	0.62		
Pure error	0.17	5	0.034		
Corrected total	75.57	18			

[a] Adequate precision = 62.579, R^2 = 0.9940, adjusted R^2 = 0.9902, predicted R^2 = 0.9645.
[b] Adequate precision = 43.803, R^2 = 0.9836, adjusted R^2 = 0.9755, predicted R^2 = 0.8974.
[c] Adequate precision = 12.166, R^2 = 0.9015, adjusted R^2 = 0.8522, predicted R^2 = 0.7483.

Accordingly, SS increased. The laser energy density was the ratio of the power to S and AD and was defined as laser input energy per unit area.[23] On the other hand, when the value of the D/T ratio was greater than 0.1264, the SS gradually decreased. This was due to the fact that when the effects of the different process parameters resulted in a higher laser energy density, and over-heating was added to the weld zone, a partial decomposition of the PP occurred. Consequently, a weak welding bond was formed. Accordingly, SS decreased.

As the result indicates, it is not suggested that a very low or high laser energy density be used. The result also indicated that the maximum SS achieved in the LTW of PP corresponded to a certain value of D/T ratio; both a too small and too large value of the molten pool D/W ratio made SS decrease.

Validation of the Developed RSM Models with the Simulated and Experimental Results
To validate the developed RSM models, three confirmation tests chosen randomly from the simulated and experimental results were conducted. The process parameters used for the simulation and EX were all within the ranges of Table IV. Table VII shows the simulated results, predicted values, actual results, and calculated percentage errors of the confirmation
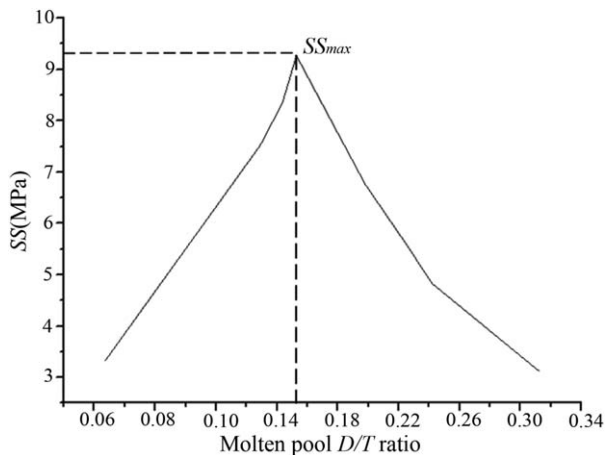
Figure 8. Matching curve of the D/T ratio and SS (SS_{max} = maximum shear strength).

tests. As the accuracy of the numerical simulation was confirmed previously, in this case, the RSM models of WW and DUL were validated by the simulated results, whereas the model of SS was validated by the experimental results. We observed that the predicted values of the responses were in good agreement with the simulated and actual results, which illustrated that the results of the developed RSM models was nearly accurate.

Figure 9(a,b) shows the respective relationship between the simulated and predicted values of the WW and DUL. The relationship between the predicted and actual value of SS is shown in Figure 9(c). The results illustrate that the developed RSM models of WW and DUL were adequate as the percentage error between the simulated and predicted values was small. At the same time, there was a small percentage error between the predicted and actual values, which showed that the developed model of SS was accurate. Therefore, these RSM models could be used to predicted the WW, DUL, and SS of the LTW process with significant accuracy.

NUMERICAL-SIMULATION-DRIVEN OPTIMIZATION OF PROCESS PARAMETERS

In this study, a multiple-response method called the *desirability function approach* was used to solve the problem of optimizing the multiobjective responses simultaneously. The statistical software Design-Expert version 8 supplied the optimization capabilities on basis of the desirability function.

Desirability Function Approach

In the desirability function approach, each estimated response (y_i) is transformed into a scale-free value, namely, the desirability value (d_i), whose value is between 0 and 1 and increased as the corresponding response value becomes more desirable. The total desirability function (DF), which is the geometric mean of the individual d_is toward the target value, is calculated and optimized. DF is defined as follows:[7]

$$DF = \left[\prod_{i=1}^{m} d_i \right]^{1/m} \qquad (9)$$

where m is the number of responses and i represents a certain response. d_i is defined as follows. If y_i is beyond the acceptable limit, the corresponding d_i will be 0. If y_i is on the target, d_i will be equal to 1. If y_i falls within the limits but not on the target, the corresponding d_i will be between 0 and 1. If y_i is close to the target, d_i will be closer to 1.

If y_i wants to be maximized, the single desirability function can be defined as:

$$d_i = \begin{cases} 0 & y_i \leq L_i \\ \left(\dfrac{y_i - L_i}{T_i - L_i} \right)^{wt_i} & L_i < y_i < T_i \\ 1 & y_i \geq T_i \end{cases} \qquad (10)$$

The desirability function can be a linear function only when the weight value (wt_i) is equal to 1. If wt_i is greater than 1, more emphasis should be required on the target. If wt_i is less than 1, less emphasis on the target should be required.

Table VII. Validation of the Predicted Values with Simulated Results

Number	P (W)	AP (W)	S (mm/s)	F (mm)		WW (mm)	DUL (mm)	SS (MPa)
1	5	3.62	3	+2	Simulated	1.28	0.550	
					Predicted	1.25	0.535	7.12
					Actual			7.65
					‖Error‖	2.34%	2.73%	6.93%
2	8	5.54	4	+3	Simulated	1.38	0.654	
					Predicted	1.41	0.633	7.79
					Actual			8.12
					|Error|	2.17%	3.21%	4.06%
3	9.2	6.45	5	+4	Simulated	1.34	0.582	
					Predicted	1.40	0.602	6.28
					Actual			6.76
					|Error|	4.48%	3.44%	7.10%
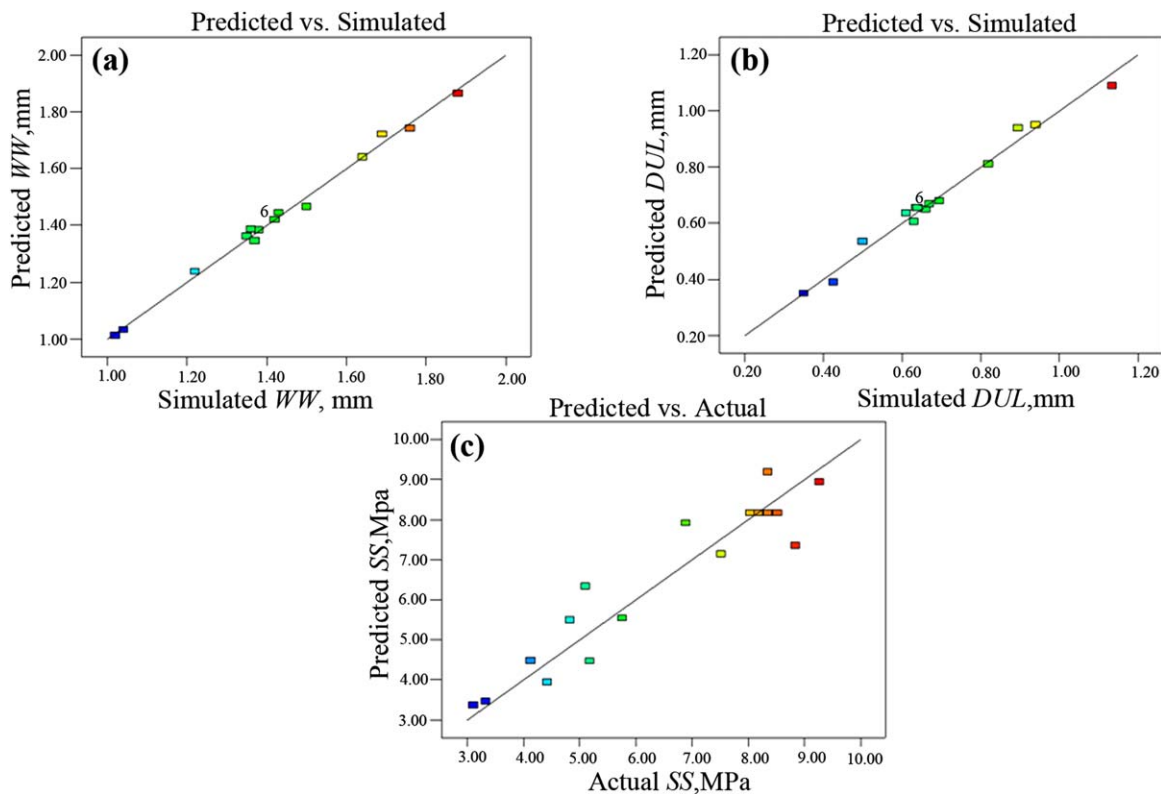
Figure 9. (a,b) Relationship between the simulated and predicted values of WW and DUL, respectively, and (c) relationship between the predicted and actual values of SS. [Color figure can be viewed in the online issue, which is available at wileyonlinelibrary.com.]

If y_i needs to be minimized, the single desirability function can be defined as follows:

$$d_i = \begin{cases} 1 & y_i \leq T_i \\ \left(\dfrac{U_i - y_i}{U_i - T_i}\right)^{wt_i} & T_i < y_i < U_i \\ 0 & y_i \geq U_i \end{cases} \quad (11)$$

where L_i represents the minimum value of the desired response, U_i represents the maximum value of the desired response, and T_i represents the target value.

RESULTS AND DISCUSSION

In the welding of microdevices field, a small WW is required, and enough SS also has to be considered. The problem of linking between WW and SS is that the increase of SS is usually accompanied by a wider and deteriorated WW as a result.[7] Meanwhile, as shown in Figure 8, in addition to achieving the same SS compared with the value of the D/T ratio, which was more than 0.1264, a D/T ratio of less than 0.1264 indicated that a relatively lower laser energy density was used in the welding.

On the basis of the results of numerical simulation and tensile EX, one criterion was introduced in this multiobjective optimization. The goal was to reach the maximum SS and minimum WW with no limitations on the D/T ratio. The optimization criterion by the method of the desirability function is shown in Table VIII.

The overall desirability can be presented by eq. (12). In this optimization, eq. (12) was used as the fitness function to estimate the suitability of each individual:[24]

$$DF = (d_1 * d_2 * d_3)^{1/3} \quad d_1 = \begin{cases} 1 & y_1 < 1.02 \\ (0,1) & 1.02 < y_1 < 1.88 \\ 0 & y_1 > 1.88 \end{cases} \quad d_2 = \begin{cases} 1 & 0.0636 \leq y_2 \leq 0.1264 \\ 0 & otherwise \end{cases} \quad d_3 = \begin{cases} 1 & y_3 > 9.27 \\ (0,1) & 3.11 < y_3 < 9.27 \\ 0 & y_3 < 3.11 \end{cases} \quad (12)$$

Table IX shows the results of the multiobjective optimization based on the criterion with the desirability function. The table presents eight groups of the optimal solutions. According to the criterion, the optimum parametric range was determined as

Table VIII. Optimization Criteria by the Desirability Function Approach

Parameter/response	y_i	L	U	Importance	Criteria
P (W)		2.5	10.5	3	In range
S (mm/s)		1	5	3	In range
F (mm)		0	4	3	In range
WW (mm)	y_1	1.02	1.88	3	Minimize
D/T	y_2	0.0636	0.1264	3	In range
SS (MPa)	y_3	3.11	9.27	3	Maximize

follows: that of P was 5.46–5.61 W, that for S was 3.25–3.37 mm/s, and that for F was +0 mm. On the whole, the process parameter combinations with the highest d_is were obtained as the best LTW conditions.

To validate the optimal results, three groups of confirmation tests were conducted and were chosen randomly from the whole optimal results. Table X summarizes the results of the confirmation tests. Fair agreement among the simulated, predicted, and

Table IX. Results of Multiobjective Optimization Using a Desirability Function Based on the Criteria

Number	P (W)	S (mm/s)	F (mm)	WW (mm)	D/T	SS (MPa)
1	5.52	3.26	+0	1.238	0.0990	8.394
2	5.53	3.37	+0	1.238	0.0990	8.394
3	5.53	3.26	+0	1.239	0.0992	8.403
4	5.50	3.25	+0	1.237	0.0989	8.388
5	5.59	3.29	+0	1.242	0.0996	8.428
6	5.46	3.25	+0	1.233	0.0983	8.350
7	5.53	3.28	+0	1.235	0.0987	8.372
8	5.61	3.31	+0	1.242	0.0995	8.422

experimental results was observed; this indicated that the optimal results were nearly accurate and the integrated (FEM–RSM–EX) approach was an effective optimization method for conducting the multiobjective optimization for the LTW process.

Table X. Confirmation Tests for Optimal Results

Number	P (W)	S (mm/s)	F (mm)		WW (mm)	D/T	SS (MPa)
				Simulated	1.230	0.0973	
				Predicted	1.246	0.1001	8.462
				|Error|	1.30%	2.88%	
				Simulated	1.230	0.0973	
1	5.58	3.26	+0	Actual	1.192	0.0942	8.031
				|Error |	3.19%	3.29%	
				Predicted	1.246	0.1001	8.462
				Actual	1.192	0.0942	8.031
				|Error|	4.53%	6.26%	5.37%
				Simulated	1.362	0.1127	
				Predicted	1.282	0.1046	8.673
				|Error|	5.87%	7.19%	
				Simulated	1.362	0.1127	
2	6.33	3.64	+0	Actual	1.258	0.1065	8.128
				|Error|	8.27%	5.82%	
				Predicted	1.282	0.1046	8.673
				Actual	1.258	0.1065	8.128
				|Error|	1.91%	1.78%	6.71%
				Simulated	1.310	0.1018	
				Predicted	1.212	0.0955	8.167
				|Error|	7.48%	6.19%	
				Simulated	1.310	0.1018	
3	5.33	3.28	+0	Actual	1.220	0.0936	7.786
				|Error|	7.38%	8.76%	
				Predicted	1.212	0.0955	8.167
				Actual	1.220	0.0936	7.786
				|Error|	0.66%	2.03%	4.89%

CONCLUSIONS

In this study, a numerical-simulation-driven optimization of the LTW process under the consideration of scattering was systemically investigated through an integrated FEM–RSM–EX approach. The following conclusions could be drawn from this investigation within the limitations and considerations of this study:

1. On the basis of the results of the measuring EX, a three-dimensional thermal model was developed to simulate the temperature field and molten pool geometric characteristic parameters in the LTW process, and the simulated results were in good agreement with the experimental results.
2. The developed mathematical models could predict the values of WW, DUL, and SS with significant accuracy, and the predicted results nearly agreed with the simulated and tensile experimental results.
3. With increasing D/T ratio, SS gradually increased to a maximum value and then decreased.
4. The optimal welding condition was realized effectively with the desirability function approach. The simulated and experimental results were consistent with the predicted results. This illustrated illustrate that the integrated FEM–RSM–EX approach was an effective optimization method for conducting the multiobjective optimization for the LTW process.

In conclusion, this integrated FEM–RSM–EX approach could play a significant guiding role in EX of the LTW process with acceptable accuracy, and in this case, the traditional artificial EX was reduced and a high welding quality was achieved.

ACKNOWLEDGMENTS

REFERENCES

1. Liu, H. X.; Wang, K.; Li, P.; Zhang, C.; Du, D. Z.; Hu, Y.; Wang, X. *J. Opt. Lasers Eng.* **2012**, *50*, 440.
2. Georgiev, D. G.; Sultana, T.; Mian, A.; Auner, G. *J. Mater. Sci.* **2005**, *40*, 5641.
3. Georgiev, G. L.; Sultana, T.; Baird, R. J.; Auner, G.; Newaz, G.; Patwa. R.; Herfurth, H. *J. Mater. Sci.* **2009**, *44*, 882.
4. Nakamura, H.; Masaki, T. *J. Jpn. Welding Soc.* **2003**, *72*, 189.
5. Bryden, B. G. *Ind. Robot Int.* **2004**, *31*, 30.
6. Juhl, T. B.; Christiansen, J. D.; Jensen, E. A. *J. Appl. Polym. Sci.* **2013**, *129*, 2679.
7. Wang, X.; Zhang, C.; Wang, K.; Li, P.; Hu, Y.; Liu, H. X. *J Opt. Laser Technol.* **2012**, *44*, 2393.
8. Acherjee, B.; Kuar, A. S.; Mitra, S.; Misra, D.; Acharyya, S. *J. Opt. Laser Technol.* **2012**, *44*, 1372.
9. Mayboudi, L. S.; Birk, A. M.; Zak, G.; Bates, P. *J. Proc. Appl. Simul. Model* **2006**, *522*, 531.
10. Mahmood, T.; Mian, A.; Amin, M. R.; Auner, G.; Witte, R.; Herfurth, H.; Newaz, G. *J. Mater. Proc. Technol.* **2007**, *186*, 37.
11. Mian, A.; Newaz, G.; Mahmood, T.; Auner, G. *J. Mater. Sci.* **2007**, *42*, 8150.
12. Acherjee, B.; Kuar, A. S.; Mitra, S.; Misra, D. *J. Opt. Laser Technol.* **2012**, *44*, 1281.
13. Ilie, M.; Kneip, J. C.; Matte, S.; Nichici, A.; Roze, C.; Girasole, T. *J. Opt. Lasers Eng.* **2007**, *45*, 405.
14. MatWeb. http://www.matweb.com (accessed June 11, 2013).
15. ANSYS User's Manual, Version 12.0; Swanson Analysis Systems, USA, 2009.
16. Mian, A.; Mahmood, T.; Auner, G.; Witte, R.; Herfurth, H.; Newaz, G. *J. Mater. Res. Soc.* **2006**, *926*, 08.
17. Acherjee, B.; Kuar, A. S.; Mitra, S.; Misra, D. *J. Eng. Sci. Technol.* **2010**, *2*, 176.
18. Montgomery, D. C. Design and Analysis of Experiments, 6th ed.; Wiley: New York, **2001**.
19. Plastics—Determination of Tensile Properties—Part 1: General Principles, German Version; EN ISO 527-1:2012; Plastics System, German, 2012.
20. Design-Expert, Version 7 2007 User's Guide, Technical Manual; Stat-Ease: Minneapolis, MN, **2007**.
21. Benyounis, K. Y.; Olabi, A. G.; Hashmi, M. S. *J. J Mater. Process Technol.* **2005**, *164–165*, 978.
22. Acherjee, B.; Misra, D.; Bose, D.; Venkadeshwaran, K. *J. Opt. Laser Technol.* **2009**, *41*, 956.
23. Mescheder, U. M.; Alavi, M.; Hiltmann, K.; Lizeau, C. H.; Nachtigall, C. H.; Sandmaier, H. *Conf. Sens. Actuators A* **2002**, *97–98*, 422.
24. Pasandideh, S. H. R.; Niaki, S. T. A. *J. Appl. Math. Comput.* **2006**, *175*, 366.